methods

Differentiating brown and white adipose tissues by high-resolution diffusion NMR spectroscopy[S]

Sanjay Kumar Verma,* Kaz Nagashima,* Jadegoud Yaligar,* Navin Michael,† Swee Shean Lee,* Tian Xianfeng,* Venkatesh Gopalan,* Suresh Anand Sadananthan,† Rengaraj Anantharaj,* and S. Sendhil Velan[1,*,†,§]

Laboratory of Molecular Imaging, Singapore Bioimaging Consortium,* and Singapore Institute for Clinical Sciences,† Agency for Science Technology and Research (A*STAR), Singapore; and Department of Physiology,§ Yong Loo Lin School of Medicine, National University of Singapore, Singapore

Abstract There are two types of fat tissues, white adipose tissue (WAT) and brown adipose tissue (BAT), which essentially perform opposite functions in whole body energy metabolism. There is a large interest in identifying novel biophysical properties of WAT and BAT by a quantitative and easy-to-run technique. In this work, we used high-resolution pulsed field gradient diffusion NMR spectroscopy to study the apparent diffusion coefficient (ADC) of fat molecules in rat BAT and WAT samples. The ADC of fat in BAT and WAT from rats fed with a chow diet was compared with that of rats fed with a high-fat diet to monitor how the diffusion properties change due to obesity-associated parameters such as lipid droplet size, fatty acid chain length, and saturation. Feeding a high-fat diet resulted in increased saturation, increased chain lengths, and reduced ADC of fat in WAT. The ADC of fat was lower in BAT relative to WAT in rats fed both chow and high-fat diets. Diffusion of fat was restricted in BAT due to the presence of small multilocular lipid droplets. Our findings indicate that in vivo diffusion might be a potential way for better delineation of BAT and WAT in both lean and obese states.—Verma, S. K., K. Nagashima, J. Yaligar, N. Michael, S. S. Lee, T. Xianfeng, V. Gopalan, S. A. Sadananthan, R. Anantharaj, and S. S. Velan. **Differentiating brown and white adipose tissues by high-resolution diffusion NMR spectroscopy. *J. Lipid Res.* 2017.** 58: **289–298.**

Supplementary key words adipose tissue • lipid droplet • diffusion spectroscopy • brown adipose tissue • white adipose tissue • magnetic resonance • fat • high-fat diet

Obesity is a global health issue, resulting in cardiovascular diseases, diabetes, hypertension, stroke, and musculoskeletal disorders (1, 2). At least two types of fat tissues exist in mammals, white adipose tissue (WAT) and brown adipose tissue (BAT), and they have different colors, cell structures, and functional roles (3–5). WAT comprises the majority of body fat, which is utilized for energy storage, whereas BAT is a minor portion that is involved in thermogenesis, due to the presence of uncoupling protein 1 (UCP1) in the mitochondria. In addition to the differences in energy storage and expenditure, BAT is a highly heterogeneous, densely vascularized tissue with abundant oxygen, blood supply, and iron-rich mitochondria (6, 7). WAT is composed of unilocular lipid droplets, whereas BAT is composed of multilocular lipid droplets scattered throughout the cytoplasm and surrounded by mitochondria.

Positron emission tomography (PET) has been the gold standard for imaging BAT (8, 9) because of a selective image contrast of activated BAT by the increased uptake of ^{18}F-deoxyglucose. However, PET is not suitable for longitudinal studies because it requires injection of exogenous radioactive tracers. Magnetic resonance (MR)-based methods are more promising for real-time and long-term observation of fat accumulation and consumption (10). Traditional MR-based approaches exploit the differences in the water content in WAT and BAT using chemical shift imaging or the Dixon technique (11–13). Imaging of water and fat permits quantitative assessment of the fat fraction. Additionally, the differences in iron content, perfusion, and vasculature have been exploited by T_2 and T_2* relaxation techniques (14, 15). However, although WAT and BAT are manually separable by color and texture, they cannot be easily distinguished by MR because of the similarity in their magnetic and chemical characteristics (14, 15).

Applications of nontraditional MR methodologies for selectively detecting BAT have been attempted. Branca and Warren (16, 17) have studied focusing on intermolecular multiple-quantum coherences through dipolar

*This work was supported by the intramural funding of the Singapore Bioimaging Consortium, A*STAR, Singapore. The authors have nothing to disclose with regard to this study.*

Manuscript received 27 September 2016 and in revised form 13 November 2016.

Published, JLR Papers in Press, November 14, 2016
DOI 10.1194/jlr.D072298

Abbreviations: ADC, apparent diffusion coefficient; BAT, brown adipose tissue; MR, magnetic resonance; PFG, pulsed field gradient; UCP1, uncoupling protein 1; WAT, white adipose tissue.

[1]To whom correspondence should be addressed.
e-mail: sendhil_velan@sbic.a-star.edu.sg

[S] The online version of this article (available at http://www.jlr.org) contains a supplement.

interactions between water and fat methyl protons. A quantitative cross-peak originating from a flip-flip or flip-flop transition can be observed in the two-dimensional MR spectra. Furthermore, a combination of intermolecular double-quantum coherence with a chemical shift encoded Dixon method has recently been reported by Bao et al. (18). The feasibility of intermolecular methodologies has apparently been verified, but the low sensitivity issue has yet to be resolved, especially for human imaging (16).

Measurement of molecular diffusion using pulsed field gradient (PFG) NMR is a way to extract the microstructural information (19). Diffusion of large molecules, such as lipids or triglycerides, in adipose tissue is influenced by several factors, including molecular weight, temperature, lipid droplet size, and chemical composition (20–24). Recently, the diffusion properties of intramyocellular (IMCL) and extramyocellular lipids in the skeletal muscle of rodents (25) and humans (26) have been investigated, and restricted diffusion has been observed in IMCL. Modeling the restricted diffusion provides a way to quantitate the lipid droplet size by using diffusion NMR with a theory for emulsions (27, 28). This approach has been utilized in vivo (25) and also in other studies involving oil-in-water emulsions (29, 30). Because of the dependence of diffusion on droplet size, WAT, with large unilocular lipid droplets, can be expected to have different diffusion properties compared with BAT, with smaller multilocular lipid droplets.

The fat composition of the adipose tissues depends on several factors, including dietary intake. The type of diet (e.g., high-fat diet) can alter the metabolism of adipose tissue, leading to metabolic diseases such as obesity and diabetes (31). Lipids are mainly triglycerides with a small amount of cholesterol and degradation products of triglycerides. Saturated, monounsaturated, and polyunsaturated triglycerides are formed through the combination of glycerol with three fatty acid molecules. The composition of saturated and unsaturated fat can play an important role in obesity and diabetes (31). It has been shown that the BAT and WAT in mice differ in the amount of saturated and unsaturated fatty acids (6). Lipid droplets are also important organelles involved in diverse functions, including energy metabolism and cell homeostasis. High-fat diets result in excessive accumulation of lipid droplets and have been associated with metabolic dysfunction leading to obesity and type 2 diabetes (32). Large lipid droplets in cardiac myocytes are also responsible for cardiac dysfunction (33). In this context, biophysical properties and the size of the lipid droplets in relation to adipose tissue expansion is essential for understanding obesity and the associated health issues.

In this report, we demonstrate and characterize the biophysical properties of BAT and WAT through quantitative translational diffusion measurements by high-resolution diffusion NMR spectroscopy at two different temperatures, 25°C and 36°C. Furthermore, the effect of high-fat diet on diffusion properties of WAT and BAT and the restricted diffusion in BAT were investigated. The droplet size distribution in BAT was estimated by modeling the restriction.

MATERIALS AND METHODS

Animals and tissue preparation

All the animal experiments and procedures were conducted according to the animal protocols approved by the local Institutional Animal Care and Use Committee. Twelve male Wistar rats (InVivos, Singapore) at 7 weeks of age were randomized into two groups: chow diet and high-fat diet. The high-fat diet was composed of 32% saturated, 36% monounsaturated, and 32% polyunsaturated fat. The normal chow diet (Altromin no. 1324 mod, Altromin, Lage, Germany) had 18% protein and 6% fat. Tissue samples were obtained from both chow and high-fat diet-fed rats at 15 weeks of age by postmortem dissection. A BAT depot was excised from the interscapular region, whereas WAT was from the gonadal fat pad. Contamination of BAT by WAT was minimized by removing the surrounding WAT that could be distinguished by the naked eye. Approximately 150–200 mg of WAT or BAT tissue was weighed after trimming with scissors and placed between Ultem (amorphous polyetherimide) susceptibility-matching plugs (SP-U-5; Doty Scientific, Columbia, SC) (34, 35) in a thin-walled NMR tube (S-5-600-7; Norell Inc., Landisville, NJ) by using a positioning rod. The sample region, which was approximately 2 mm thick, was carefully positioned to the center of the detection coil by using a sample-height gauge. Fresh BAT and WAT samples were examined within 5 h after surgery by keeping them at 4°C before runs.

NMR data acquisition and analysis

Ex vivo NMR experiments were performed on an AVANCE III NMR spectrometer, and the data were processed by using Topspin 3.2 software (Bruker Biospin GmBH, Rheinstetten, Germany). A standard 5 mm indirect detection broadband probe head with an actively shielded z-gradient coil (Bruker) was set in a 54 mm vertical bore 9.4 T superconducting magnet. The static field shim coil settings were manually adjusted using the sample itself by observing the Fourier-transformed ^{1}H NMR spectrum with repetition of data acquisitions using a short relaxation delay and a small pulse flip angle. The maximum attainable field gradient was 53.9 Gauss/(cm rad) at 10 A of coil current, which was the maximum output of a driver unit. The 90° pulse width was 9.6 μs at 10 W of the transmitter power setting. The signal detection region was thermostated at 25.0 ± 0.1°C and 36.0 ± 0.1°C with dried air and a heater. The deuterium field lock was turned off during the whole measurement processes, and the lock amplitude and sweep settings were minimized to prevent undue field drifts. A total of 1,024 data points were acquired for a free induction decay to cover a spectral width of 20 parts per million (ppm) with an acquisition time of 0.064 s. The relaxation delay (d_1) was set to 15 s, which ensured a magnetization recovery time of 10 × T_1. The transmitter offset was set near the center of the whole spectral width with an arbitrary, easy-to-remember offset setting value (400.13 MHz + 1,300 Hz). All resonances were assigned with reference to the water signal at 4.70 ppm. The one-dimensional spectra were acquired with a 90° pulse. The translational diffusion was measured with a bipolar-stimulated echo sequence (36). The signal decay is given by the Stejskal-Tanner equation (37):

$$S = S_0 e^{-\gamma^2 G^2 \delta^2 \left(\Delta - \frac{\delta}{3} - \frac{\tau}{2}\right) D} = S_0 e^{-bD} \qquad \textit{(Eq. 1)}$$

where γ is the gyromagnetic ratio of nuclei observed (rad/T/s), G is the gradient strength (T/m), δ is the field gradient pulse width (s), and τ is the interval for switching the polarization of the field gradient pulse (s). For bipolar gradient diffusion pulse

sequences, the reduced diffusion time is defined by $\Delta_r = \Delta - \delta/3 - \tau/2$ (36). D is the translational diffusion coefficient that corresponds to the slope of a semilogarithmic intensity decay plot against b values. A total of 16 spectra were acquired with exponentially increasing gradient strength (2% to 96%), while keeping Δ = 500 ms, δ = 6 ms, and τ = 0.5 ms, which resulted in minimum and maximum b values of 0.0149×10^4 s/mm^2 and 35.88×10^4 s/mm^2, respectively. The fitting was performed with 14 spectra (maximum b values $\sim 12.7 \times 10^4$ s/mm^2) to obtain the sufficient goodness of fit $R^2 \cdot 0.95$ and optimal diffusion coefficient. Additional sets of experiments were performed on the same tissue samples with a longer diffusion time (Δ = 0.25, 0.5, 1, and 2 s) with gradient pulse width (δ = 10 ms) and gradient polarization switching interval (τ = 0.5 ms) to investigate the restricted diffusion. Appropriate logarithmically spaced gradient strength was used for the minimum and maximum b values of $\sim 0.08 \times 10^4$ and 48.9×10^4 s/mm^2, respectively. The gradient strength was calibrated with a trace amount of HDO in D_2O at 25°C (38, 39). To calibrate the gradient, a total of 10 spectra were acquired with Δ = 100 ms, δ = 3 ms, and τ = 0.5 ms with increasing gradient strength (2% to 30%), which corresponded to the maximum b values of $\sim$1,668 s/mm^2. A rectangular gradient pulse was used for the encoding and decoding throughout all diffusion measurements. All NMR experiments were performed both at room temperature (25°C) and at physiological temperature (36°C).

The spectral area under the most prominent fat (-CH_2-) peak at $\sim$1.3 ppm was integrated by using Topspin software. The apparent diffusion coefficient (ADC) was calculated by fitting the experimental data to equation 1 by using the Levenberg-Marquardt least-square curve fitting function *lscurvefit* of MATLAB® R2010b (The MathWorks, Inc., Natick, MA). A custom Levenberg-Marquardt nonlinear least-squares algorithm-based fitting routine was developed to compute the peak areas by modeling the water and lipid peaks in the ^{1}H spectrum as a sum of Gaussian peaks. Mean chain length, saturation, and unsaturation indices were computed by using the equations as reported in the literature (40).

Histopathologic assessment of interscapular tissues

The BAT samples from the interscapular area were dissected from the rats, as described by Lim et al. (41). The gonadal WAT from the abdominal area and the rhomboideus muscle around the interscapular area were also collected. All tissue samples were fixed in 10% neutral buffered formalin for 24 h and dehydrated before embedding in paraffin wax. Tissue sections were sliced at 5 μm and mounted on positively charged glass slides and then stained with hematoxylin and eosin (H and E). Brightfield whole-slide images were captured at ×20 optical magnification with an Aperio ScanScope CS instrument (Leica Biosystems, Nussloch, Germany).

mRNA analysis

RNA was extracted from the BAT, WAT, and muscle samples by using the RNeasy Lipid Tissue Mini Kit (Qiagen 74804) and treated with DNase I prior to cDNA conversion by using a revertAid H minus first-strand cDNA synthesis kit (Thermo Scientific k1632) with oligo d(T) 18 primer according to the manufacturer's instructions. For real-time quantitative PCR, cDNA samples were analyzed in triplicate by using the SYBR Green PCR Master Mix reagent kit (Applied Biosystems 4367659) on a StepOnePlus Real-Time PCR System (Applied Biosystems). Relative mRNA levels were calculated and normalized to β-actin (primer sequences: CCGCGAGTACAACCTTCTTGC and TCGTCATCCATGGCGAACTGG), which was used as an endogenous control gene. The primer sequences used for the UCP1 measurements were ATCTTCTCAGCCGGCGTTTC and CTTGGATCTGAAGGCGGACTTT. The UCP1 expressions in BAT and WAT from chow and high-fat diet tissues were normalized with respect to the expression in muscle.

Droplet size distribution

The lipid droplet size distribution can be assessed by modeling the restricted diffusion behavior, as described by Murday and Cotts (27). Assuming the rapid convergence of the Bessel function, a simplified expression shown in equation 2 was derived by Garasanin et al. (29) and utilized for various applications (25, 30):

$$S(R) = S_0(R) exp\left[-\frac{54 g^2 R^2 \gamma^2 \left[3\left\{ \exp\left(-\frac{13D(\Delta-\delta)}{3R^2}\right) - 2\exp\left(-\frac{13D\delta}{3R^2}\right) - 2\exp\left(-\frac{13D\Delta}{3R^2}\right) + \exp\left(-\frac{13D(\Delta+\delta)}{3R^2}\right) + 2\right\} R^2 - 26D\delta \right]}{15379D^2} \right] \quad \textit{(Eq. 2)}$$

where $S(R)$ and $S_0(R)$ are the signals obtained with and without diffusion gradient from the droplet size of radius R, respectively, and D is free lipid diffusion coefficient. Considering the heterogeneity of the lipid droplets in BAT, the size distribution is assumed to be log-normal as:

$$P(R) = \left(\frac{1}{\sigma\sqrt{2\pi}}\right) \frac{exp\left[-\frac{\left(ln(2R) - ln(2R_0)\right)^2}{2\sigma^2} \right]}{2R} \quad \textit{(Eq. 3)}$$

where σ is the standard deviation of $\ln(2R)$. The observed signal (S_{obs}) in PFG diffusion experiments is the volume-weighted average signal over all the droplets in whole sample and is described by the probability distribution function expressed as:

$$S_{obs} = \frac{\int S(R) R^3 P(R) dR}{\int R^3 P(R)} \approx \frac{\sum_{R_{min}}^{R_{max}} S(R) R^3 P(R)}{\sum_{R_{min}}^{R_{max}} R^3 P(R)} \quad \textit{(Eq. 4)}$$

where the denominator is a normalization constant, and R_{min} and R_{max} are the minimum and maximum droplet radii, respectively. The NMR signal attenuation at diffusion time of 2 s was fitted to equation 4 with a nonlinear least-squares fit (MATLAB® R2010b) to obtain the mean radius, R_0, and the polydispersity or variance of the BAT droplet, σ. Automated analysis of H-and-E-stained slides of WAT sections was performed by using Adiposoft, a fully automated open-source plugin of Fiji software (42, 43), to quantify the number and size of droplets.

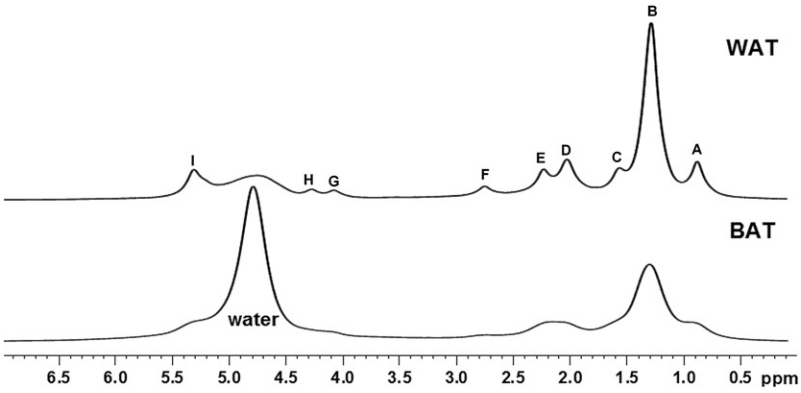

Fig. 1. ^{1}H spectra of BAT and WAT at 25°C. The proton NMR spectra were acquired from chow diet BAT and WAT. The fat resonances include -C**H**$_3$-(CH$_2$)n (A), -(C**H**$_2$)n- (B), -CH$_2$-O-CO-CH$_2$-C**H**$_2$- (C), -CH$_2$-C**H**$_2$-CH=CH- (D), -CH$_2$-O-CO-C**H**$_2$-CH$_2$- (E), –CH=CH-C**H**$_2$-CH=CH- (F), -C**H**$_2$-O-C(O)-CH$_2$-CH$_2$- (G), -C**H**$_2$-O-C(O)-CH$_2$-CH$_2$- (H), and -C**H**=C**H**- (I) groups at ∼0.9, ∼1.3, ∼1.6, ∼2.03, ∼2.25, ∼2.76, ∼4.1, ∼4.9, and ∼5.3 ppm, respectively.

Statistical analysis

The Mann-Whitney *U* test was used to analyze the statistical significance between the chow and high-fat data using a statistical package for social sciences (SPSS, version 23.0; SPSS, Inc., Chicago, IL). All data were expressed as the mean ± standard deviation (SD) unless stated, and significance was accepted at $P < 0.05$ (*) and $P < 0.01$ (**).

RESULTS

Representative ^{1}H NMR spectra of BAT and WAT of chow diet are shown in **Fig. 1**. Even with a tissue sample that is magnetically and structurally inhomogeneous, one can obtain a reasonably high resolution with the use of commercial plastic plugs. Only a small amount of tissue,

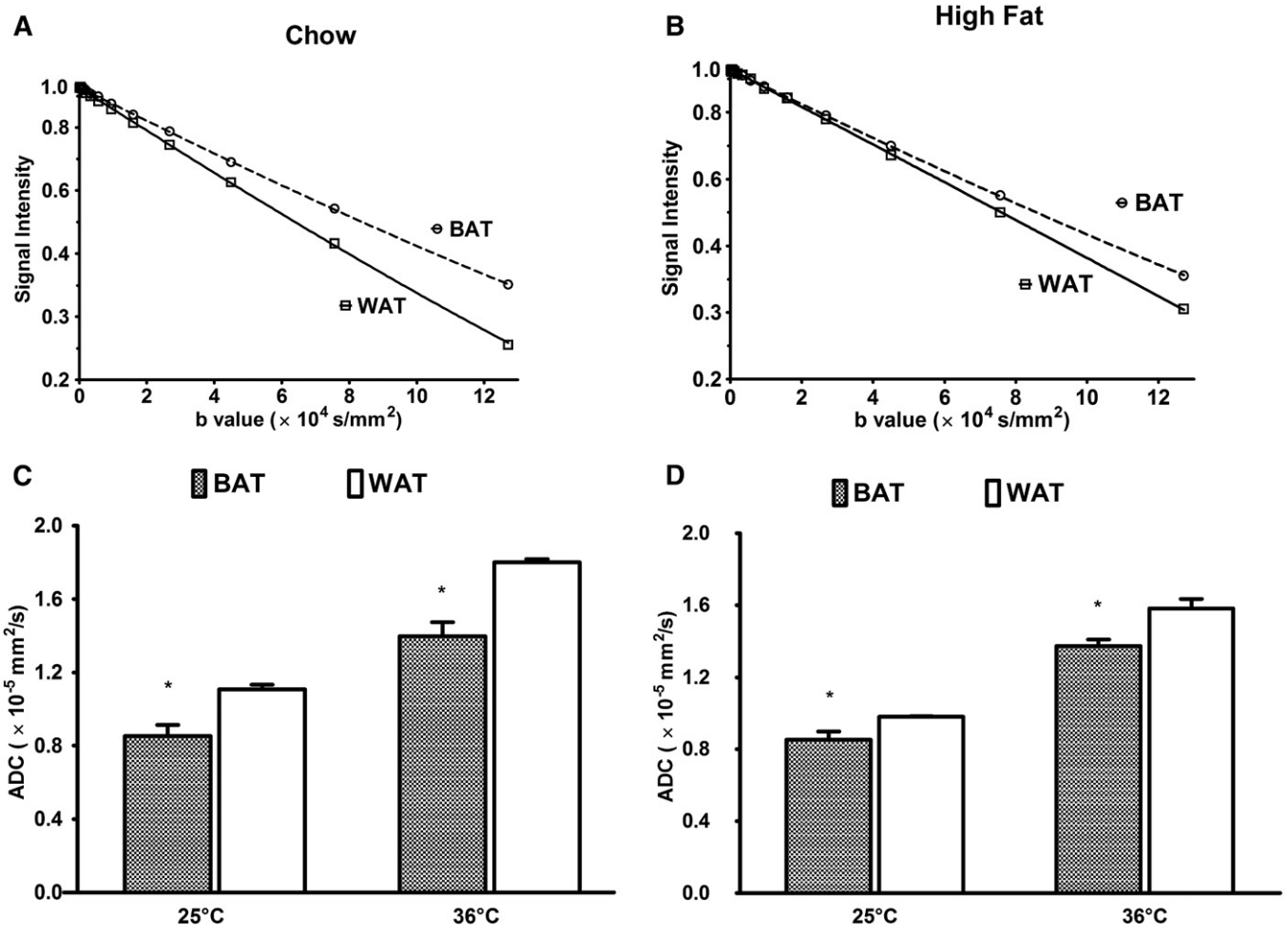

Fig. 2. Signal attenuation and ADC of BAT and WAT in the chow and high-fat groups. Semilogarithmic plots of the signal decay for various *b* values and ADC are shown for the chow and high-fat cases. Diffusional decays of the fat signal in the WAT and BAT spectra (Δ = 500 ms; δ = 3 ms; τ = 0.5 ms) for chow (A) and high-fat diet (B) are shown. The ADCs are shown for 25°C and 36°C for chow (C) and high-fat diet (D). Data are presented as the mean ± SD. * $P < 0.05$.

which is approximately 2 mm high in a 5 mm NMR tube, is necessary for the signal observation. A much better spectral resolution can typically be achieved with a WAT sample than a BAT sample, probably because of the more homogeneous tissue structure of WAT and the higher iron content in BAT. The water peak (~4.7 ppm) is dominant in the BAT spectrum, indicating that the water content was significantly higher in BAT than WAT. The *n*-methylene $-(CH_2)_n-$ signal is dominant in the WAT spectra compared with BAT, reflecting the increased fat fraction. Other prominent resonances include methyl signal $-CH_3$ (~0.9 ppm), α-methylene $-CH_2-COO$ (~2.10 ppm), allylic methylene $-CH_2-CH=CH-$ (~2.03 ppm), and olefinic –CH=CH- (~5.3 ppm) groups.

The comparison of ADC is shown within chow and high-fat diet for BAT and WAT in **Fig. 2**. The semilogarithmic diffusion signal decays acquired at 25°C in the chow and high-fat diet-fed BAT and WAT as a function of *b* values are shown in Fig. 2A, B. Figure 2C, D shows the ADC of WAT and BAT at 25°C and 36°C for both chow and high-fat diet. An increase in the ADC values for both chow and high-fat diet tissues was observed with increase in temperature. There was a significant difference in ADC between BAT and WAT in the both high-fat and chow groups. In both groups, the ADC of fat in BAT is significantly ($P < 0.05$) lower than WAT. This significant reduction in diffusion is due to the smaller multilocular droplets in BAT compared with the large unilocular droplets in WAT. By high-fat diet, a significant reduction in the fat ADC values was observed in WAT, but there was essentially no change in BAT. As a result, the difference in the ADC values between BAT and WAT became smaller for the high-fat diet cohort than for the chow diet cohort.

The data shown in Fig. 2 are reorganized in **Fig. 3A, B** to highlight the effect of high-fat diet on the ADC in BAT and WAT. The ADC values in WAT are significantly reduced in the high-fat group compared with the chow group. There were no significant changes in the ADC values in BAT. Fig. 3 demonstrates the saturation index (Fig. 3C), unsaturation index (Fig. 3D), and mean chain length (Fig. 3E) computed from the ^{1}H NMR spectra of BAT and WAT for the chow and high-fat diet-fed cohorts. The WAT tissues from high-fat diet rats exhibited significantly lower unsaturation and higher saturation indices ($P < 0.01$). A similar trend was also observed in case of BAT, but it was not significant. An increasing trend of mean chain length was observed in WAT for the high-fat diet group.

Figure 4A, B shows the signal decays as a function of the *b* value for the chow and high-fed groups observed at different diffusion times ($\Delta = 0.25$ ~2 s) at 25°C. When Δ was increased, BAT fat in both the chow and high-fat groups demonstrated a clear upward drift of the decay curves. An upward drift was observed in the presence of restricted diffusion (44, 45), whereas a downward drift was observed in a

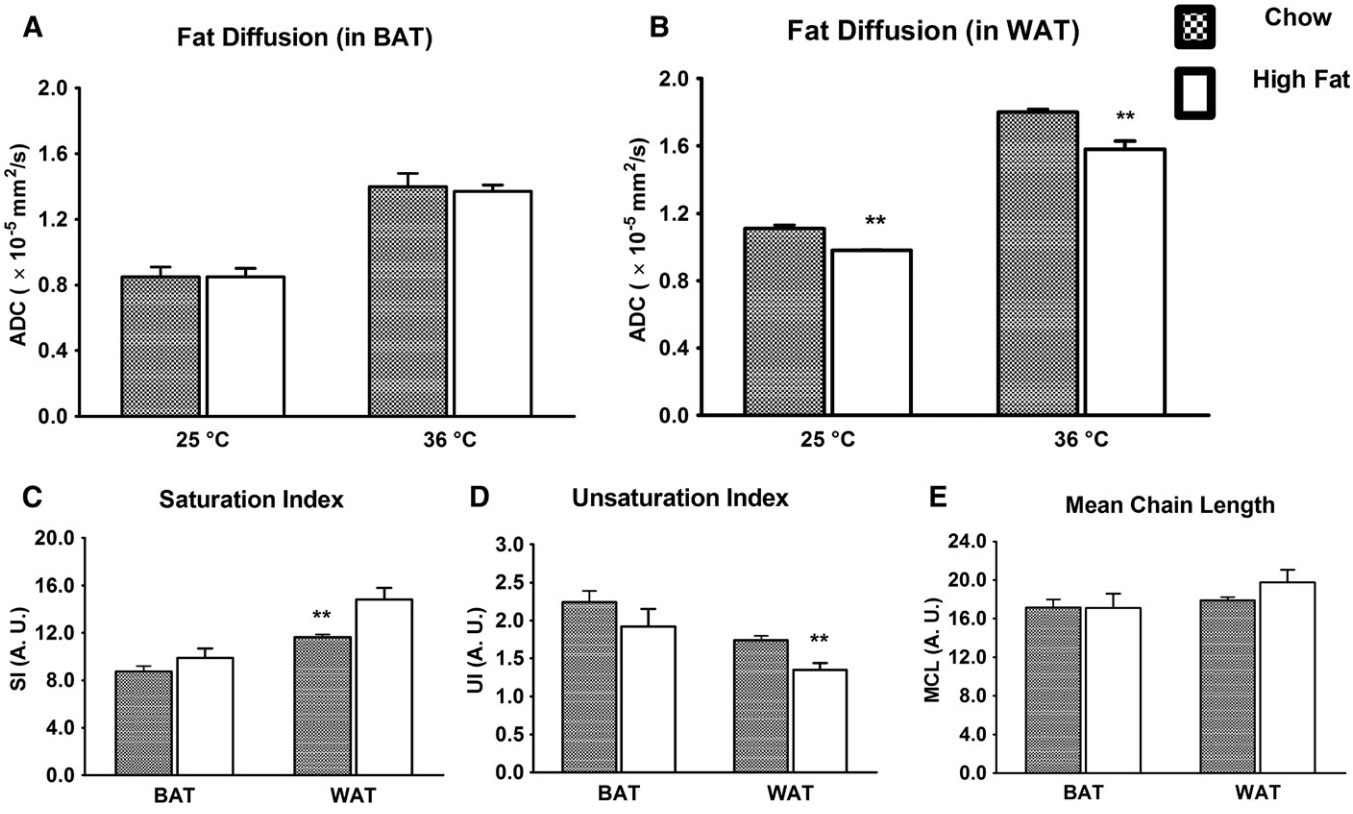

Fig. 3. Effect of high-fat diet on fat diffusion, saturation, unsaturation index, and mean chain length. A: The BAT sample did not show any significant change in ADC for chow and high-fat tissues. B: The high-fat diet resulted in a significant reduction of the fat ADC in WAT. The high-fat diet WAT exhibited a significantly ($P < 0.05$) increased saturation index (C) and a reduced unsaturation index (D). A similar trend was observed in BAT, but not as significant as in WAT. E: The mean chain length did not essentially change in BAT, whereas it increased in WAT. Data are presented as the mean ± SD. ** $P < 0.01$.

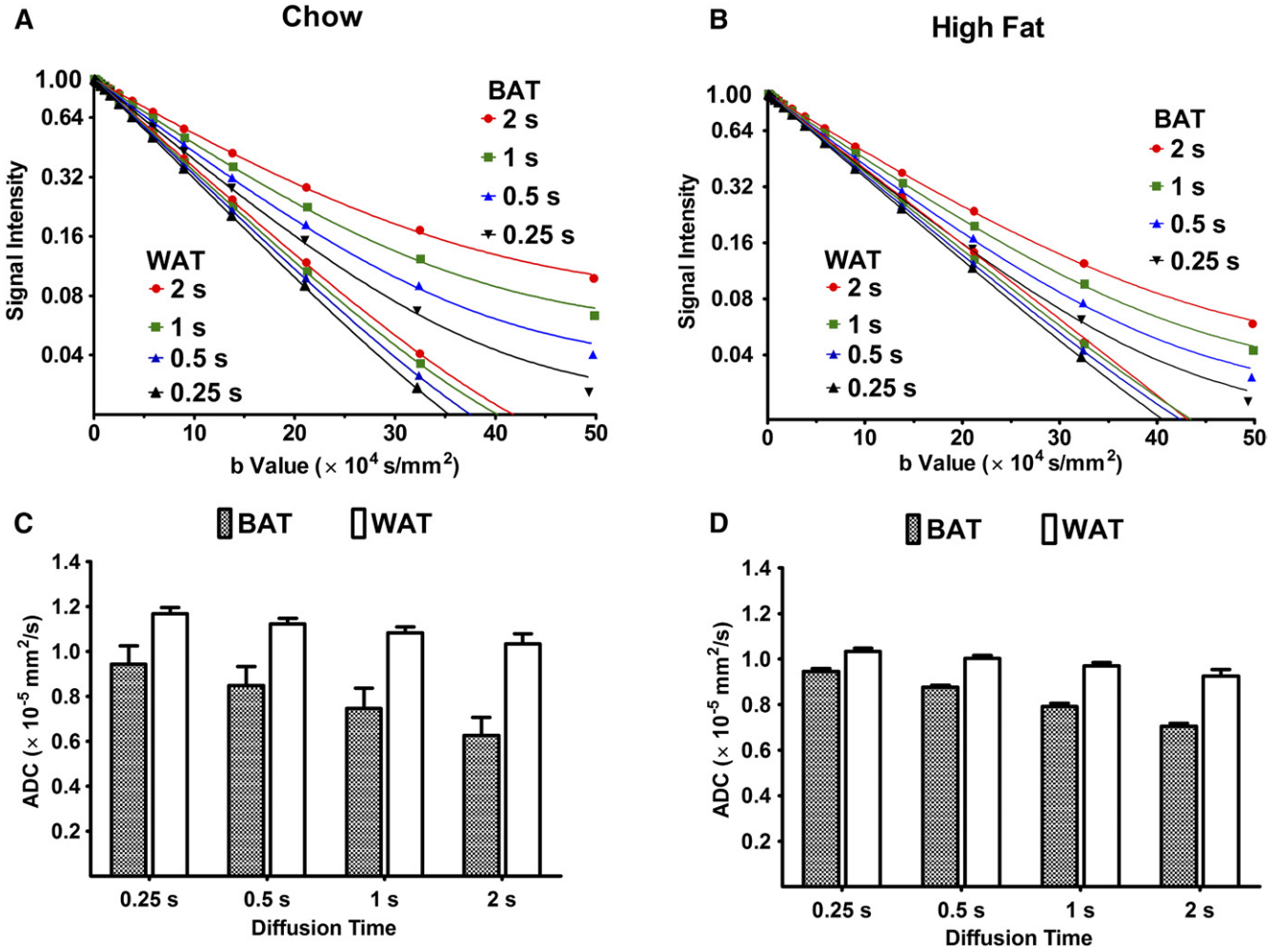

Fig. 4. ADC measurements with increasing diffusion times to investigate restriction. A and B: Diffusional signal decays in WAT and BAT with different diffusion times (Δ) are shown. The field gradient pulse width (δ/2) and the polarization changing delay (τ) were fixed to 5 and 0.5 ms, respectively. As the diffusion time was increased, a clear upward drift in the signal decay curves was seen, in the case of BAT only, and the WAT data nearly overlap, by contrast. A similar trend was observed at 36°C (data not shown). ADC corresponding to variable diffusion times was calculated with equation 1. C and D: Reduction of fat ADC with increasing diffusion time was much more significant for BAT compared with WAT.

system involving a two-site exchange (46, 47). A clear drift was not observed with WAT samples, and the data points at different Δ nearly overlapped. The high-fat BAT demonstrated a smaller upward drift compared with the chow-diet BAT, indicating relatively freer diffusion of fat molecules in high-fat BAT than in chow BAT. A similar trend was observed at 36°C in both groups (data not shown). The ADC values for these diffusion times are shown in Fig. 4C, D. WAT did not show significant changes in ADC with a change in diffusion time from 0.5 to 2 s, whereas BAT demonstrated a significant reduction in ADC. These findings indicate that the diffusion of fat molecules was restricted in BAT, whereas it was relatively free in WAT. Additionally, the high-fat diet could lead to the formation of large droplets in BAT.

Figure 5 demonstrates the H-and-E-stained section of BAT and WAT of the chow (Fig. 5A, C) and high-fat (Fig. 5B, D) diet groups. BAT exhibited smaller-sized adipocytes with a considerable volume of cytoplasm. Adipocytes of the WAT had a scant ring of cytoplasm surrounding a single large lipid droplet with an eccentric nucleus within the cell. The increase in the size of the lipid droplets in WAT of the high-fat diet was significant compared with the chow diet because of large lipid accumulation within the cell. The increase in lipid droplet size of BAT was not as significant as WAT, probably reflecting the active metabolic characteristics of BAT that utilizes the lipids as metabolic precursors. Figure 5E demonstrates the real-time PCR mRNA expression analysis of the UCP1 gene in BAT, WAT, and muscle tissues of the chow diet group. UCP1 expression was significantly higher in BAT compared with WAT in both chow and high-fat diet tissues.

Figure 6 demonstrates the fitting of signal decays and the determination of the droplet size in chow and high-fat diet BAT. Figure 6A demonstrates the fitting of diffusion attenuation of fat signal in BAT with diffusion time Δ = 2 s by the model described using equations 2–4. Figure 6B demonstrates the log-normal distribution of the fat droplet size in BAT estimated from the optimized fitting parameters of chow and high-fat tissues at diffusion time Δ = 2 s. The distribution curve was discretized to 64 intervals within the radius range of 0.1 to 5 μm. An increase in the mean of distributions was observed for high-fat diet BAT, which is consistent

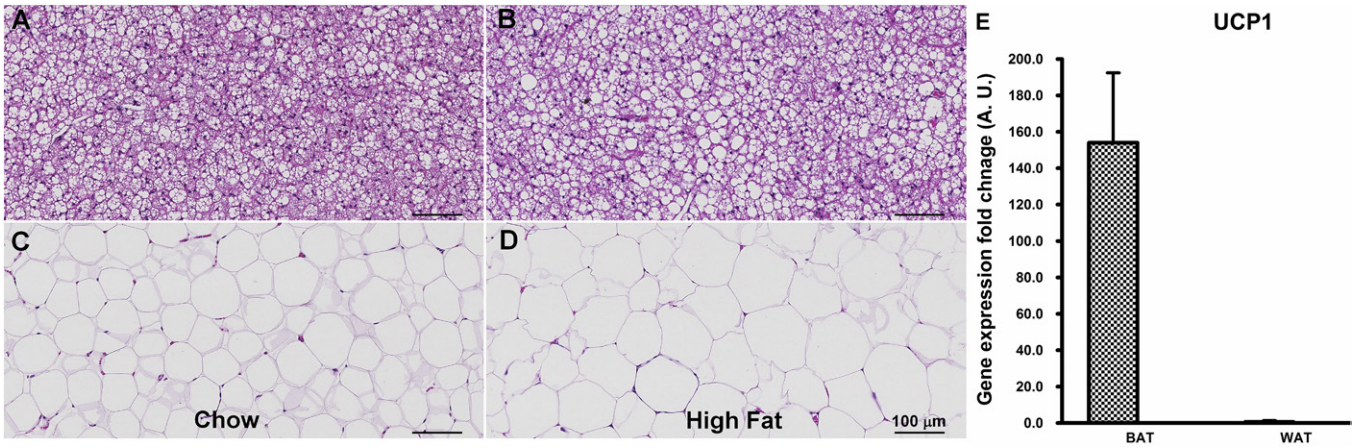

Fig. 5. H-and-E-stained optical images of BAT and WAT of chow and high-fat diet and UCP1 expression in chow diet. H-and-E staining delineates the adipocyte contours in chow diet (A) and high-fat diet (B) BAT. High-fat diet resulted in a slight increase in adipocyte sizes. Alternatively, a large size increase was observed in WAT adipocytes for high-fat diet tissues (D) compared with the chow diet (C). E: mRNA expression of the UCP1 gene was significantly higher in BAT compared with WAT.

with the histological data shown in Fig. 5. The diameter and the polydispersity of the log-normal distribution of chow and high-fat diet BAT are shown in **Table 1**. At diffusion time Δ = 2 s, the droplet diameter (polydispersity) was estimated to be 4.04 ± 0.70 (0.40 ± 0.28) μm for chow diet BAT and 4.62 ± 0.10 (0.26 ± 0.10) μm for high-fat diet BAT, respectively.

Figure 7 demonstrates the results of the automatic droplet size analysis of WAT. Figure 7A, B shows the boundaries of segmented droplets overlaid on the histological sections of chow and high-fat tissues shown in Fig. 5C, D. A total of 436 WAT droplets from the chow tissues and 217 droplets from the high-fat tissues estimated from five histological sections were identified after the automatic segmentation. Fig. 7C, D show the histograms of chow and high-fat tissues plotted with a 10 μm bin size. The mean droplet size of WAT was 27.8 ± 11.8 μm for the chow diet and 34.6 ± 16.9 μm for the high-fat diet.

DISCUSSION

The adipose tissues are the major storage sites for fat in the form of triglycerides. BAT (fat-burning tissues) and WAT (fat-storing tissues) are the two broad types of adipose tissues that play important roles in obesity. From the important role of BAT metabolism in obesity, there is a large interest in understanding the biophysical and metabolic properties by noninvasive-imaging approaches. Several groups have made ongoing efforts in investigating BAT metabolism by multimodal imaging approaches (48, 49). In the present study, BAT and WAT obtained from chow and high-fat diet-fed rats were characterized by diffusion NMR spectroscopy. Further analysis was performed to investigate restricted diffusion behavior and droplet size distribution.

The ^{1}H spectra of BAT demonstrated a stronger water resonance compared with WAT, due to the abundant intracellular and extracellular water (Fig. 1). Conversely, WAT demonstrated increased strength of fat resonances compared with BAT. Earlier MRI and MR spectroscopy studies of BAT and WAT demonstrated a decrease in the fat fraction of BAT compared with WAT (15, 50–52). The various resonances of fatty acyl chains of tissue triglycerides from BAT and WAT in the spectra permit the estimation of saturation, unsaturation, and mean chain lengths (40, 52). As shown in Fig. 3, these parameters, that is, the molecular

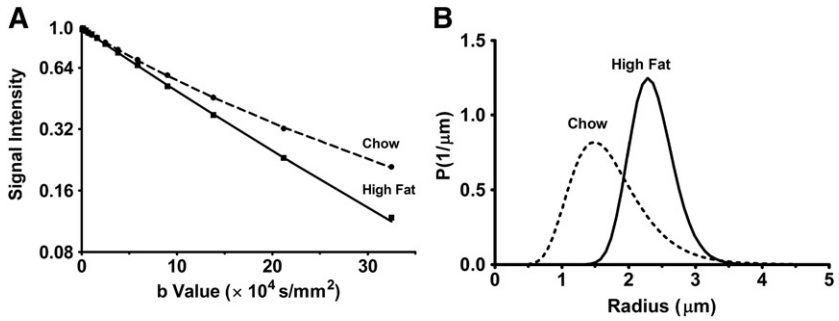

Fig. 6. Fitting of the diffusional decays of the BAT signals with the Murday-Cotts equation and calculated droplet size distribution. A: The dotted lines (chow) and full lines (high-fat) show the nonlinear least square fitted signal decay for Δ = 2 s. B: The calculated log-normal distributions of the droplet size estimated from the corresponding best parameters in chow and high-fat tissues are displayed. The distribution curves were discretized to 64 intervals within the radius range of 0.1 to 5 μm.

TABLE 1. Lipid droplet diameter for chow and high-fat diet BAT

Diet	Diameter (μm)	Variance
Chow	4.04 (0.70)	0.40 (0.28)
High-fat	4.62 (0.10)	0.26 (0.10)

Diffusion time Δ = 2 s. Values in parentheses represent the SD.

structure of fat molecules in BAT, were apparently not significantly influenced by high-fat diet as much as in WAT. The changes for BAT (WAT) were 13.2% (27.5%) for the saturation index, 14.4% (22.3%) for the unsaturation index, and 0.4% (10.5%) for the mean chain length, respectively. These changes may be due to the changes in activity of adipocytes in WAT (40).

The overall trend of fat diffusion observed in this study was not influenced by temperature (Fig. 2), although the ADC increased due to thermal energy (20). The high-fat diet did not influence the ADC of fat molecules in BAT at both ambient and physiological temperatures, whereas it reduced the ADC in WAT significantly. This is probably due to increased saturation, decreased unsaturation ($P < 0.01$), and increased mean chain length (Fig. 3C, E). The diffusion coefficient of fat molecules decreased with increases in mean chain length (53). Lipids with reduced unsaturation are stiffer and viscous, and are very likely to exhibit slower diffusion (54).

The differences in the intracellular and extracellular environment, including cellular and subcellular barriers, alter the diffusion properties, in terms of restriction. Earlier work using a Monte Carlo simulation has shown that the apparent diffusion of lipid molecules becomes fast when the droplet size increases and slows down when a long diffusion time is set (24, 25). Diffusion of fat molecules in WAT is relatively free, whereas it is restricted in BAT (Fig. 4C). This restricted behavior in BAT might be due in part to the heterogeneity of the complex multilocular droplet distribution. The microscopic geometric differences between BAT and WAT result in the significant difference of ADC values for both chow and high-fat groups (Fig. 2). The decline in ADC with a longer diffusion time became less significant in the high-fat diet BAT than in the chow diet, possibly indicating freer diffusion in the former, due to changes in cellular and subcellular barriers (Fig. 4D).

A rough estimate of the diffusion length of fat molecules is possible by assuming a simple one-dimensional path (20),

$$\bar{l} = \sqrt{2D\Delta} \qquad \textit{(Eq. 5)}$$

From Fig. 4C, the diffusion coefficient in WAT at 25°C is $\sim 1.03 \times 10^{-5}$ mm^2/s, so Δ = 2 s yields the diffusion length of 6.4 μm. Because the longitudinal relaxation time of fat molecules in BAT was approximately 650 ms (data not shown), the experimentally accessible longest diffusion time was Δ = 2 s, and a further increase, say, Δ = 5 or 10 s, was experimentally counterproductive. We assume here that almost all of the fat molecules within a droplet in BAT hit the boundary during 2 s at least once, and the experimental decay curve at Δ = 2 s represents the asymptotic

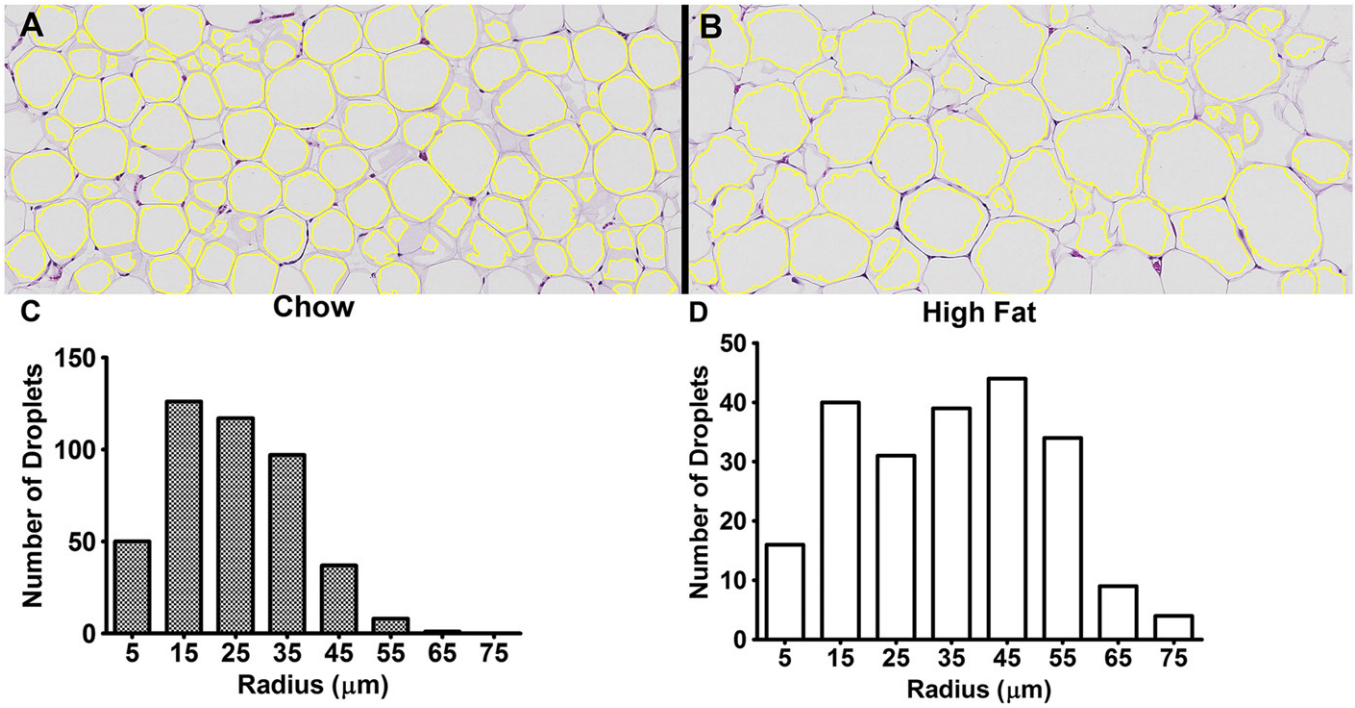

Fig. 7. Droplet size quantitation of WAT. Automatic droplet size quantification of chow and high-fat WAT using the Adiposoft plugin are shown. The boundaries of segmented droplets are overlaid on the histological section of chow (A) and high-fat (B) images. A total of 436 chow (24.8 ± 11.8 μm) and 217 high-fat (34.6 ± 16.9 μm) droplets from five histological sections of different animals were analyzed. The histograms with a bin size of 10 μm of chow (C) and high-fat (D) cases are shown. A significant ($P < 0.001$) increase in the droplet size was observed in high-fat WAT.

values obtained at a very long diffusion time. Table 1 demonstrates the droplet diameter estimation for BAT by fitting the NMR diffusion data based on the Murday-Cotts model (Fig. 6). The calculated distribution was relatively narrow and close to a Gaussian shape, rather than a log-normal shape, within the 0 to 5 μm range. The calculated apparent diameter is approximately 4 μm and found that, retrospectively, our previous assumption that $\Delta = 2$ s was sufficient to nearly cover up the diffusion distance. This verifies our use of the Murday-Cotts equation. In any case, different from hard-shelled industrial oil-in-water emulsions, some leakage of fat molecules from the droplets should exist within BAT, because they are designed to be consumed quickly during adaptive thermogenesis. This would be reasonable because, otherwise, fat molecules would not be transferred and burned in swift energy generation. Table 1 demonstrates that the apparent droplet diameter increased approximately 15% by high-fat diet. The presence of small brown droplets and large "white-like droplets" within BAT was confirmed by the histology results (Fig. 5B). The NMR diffusion-based size data are therefore consistent with the histological data. Within an experimentally feasible diffusion time (i.e., less than 5 s due to spin relaxation) restricted behavior could be observed only in BAT, not in WAT. The modeling of the restricted behavior to estimate droplet size distribution requires a large curvature in the diffusion NMR intensity profiles and a long diffusion time, enough to allow fat molecules to hit the droplet boundary.

Conversely, the size of droplet in WAT (Fig. 7) increased in the high-fat diet due to increased fat storage, which was also observed in the histological sections of WAT (Fig. 5D). Adipocyte hypertrophy because of a high-fat diet is associated with insulin resistance (55). Noninvasive measurement of lipid-droplet size distribution is a potential way to investigate hyperplastic and hypertrophic expansion of adipose tissues. PFG NMR diffusion methods can also be extended to investigate dynamic lipid droplet remodeling during BAT activation with metabolic interventions. Indeed, the triglycerides in adipose tissues have high molecular masses, so that their diffusion study requires large b values to cope with the slow diffusion. However, apart from the hardware and technical issues, a higher MR signal may be observed from BAT than from WAT by use of diffusion weighting because the signal of the latter dwindles faster as gradient strength and diffusion time increase. These advantages cannot be realized by use of spin relaxation because the spin relaxation of fat and water is faster in BAT than in WAT and the differences in T_1, T_2, or T_2* are not large.

CONCLUSIONS

In summary, we have demonstrated the differences in the biophysical properties of BAT and WAT by diffusion NMR spectroscopic techniques and studied the effect of high-fat diet on the diffusion in these two major adipose tissues. The diffusion properties of WAT were also mediated by the changes due to saturation, unsaturation, and mean chain lengths. The PFG method can be easily implemented on all NMR systems with the field gradient capability and can be used for evaluating brown or even other colored adipose tissues with metabolic alterations. This study envisages future projects involving animal and human fat research in vivo. The requirement of large b values for achieving reliable signal attenuation might be a limitation for clinical systems with the currently available gradient strengths.

The authors thank Drs. Bhanu Prakash and Krishnarao Doddapuneni for their support and discussion.

REFERENCES

1. Haththotuwa, R. N., C. N. Wijeyaratne, and U. Senarath. 2013. Worldwide epidemic of obesity. *In* Obesity. A Ticking Time Bomb for Reproductive Health. T. Mahmood and S. Arulkumaran, editors. Elsevier, Oxford, UK. 3–11.
2. Mitchell, S., and D. Shaw. 2015. The worldwide epidemic of female obesity. *Best Pract. Res. Clin. Obstet. Gynaecol.* **29:** 289–299.
3. Cinti, S. 2006. The role of brown adipose tissue in human obesity. *Nutr. Metab. Cardiovasc. Dis.* **16:** 569–574.
4. Frühbeck, G., S. Becerril, N. Sáinz, P. Garrastachu, and M. J. García-Velloso. 2009. BAT: a new target for human obesity? *Trends Pharmacol. Sci.* **30:** 387–396.
5. Nedergaard, J., and B. Cannon. 2013. How brown is brown fat? It depends where you look. *Nat. Med.* **19:** 540–541.
6. Strobel, K., J. van den Hoff, and J. Pietzsch. 2008. Localized proton magnetic resonance spectroscopy of lipids in adipose tissue at high spatial resolution in mice in vivo. *J. Lipid Res.* **49:** 473–480.
7. Hu, H. H., D. L. Smith, K. S. Nayak, M. I. Goran, and T. R. Nagy. 2010. Identification of brown adipose tissue in mice with fat-water IDEAL-MRI. *J. Magn. Reson. Imaging.* **31:** 1195–1202.
8. Cypess, A. M., S. Lehman, G. Williams, I. Tal, D. Rodman, A. B. Goldfine, F. C. Kuo, E. L. Palmer, Y-H. Tseng, A. Doria, et al. 2009. Identification and importance of brown adipose tissue in adult humans. *N. Engl. J. Med.* **360:** 1509–1517.
9. Virtanen, K. A., M. E. Lidell, J. Orava, M. Heglind, R. Westergren, T. Niemi, M. Taittonen, J. Laine, N-J. Savisto, S. Enerbäck, et al. 2009. Functional brown adipose tissue in healthy adults. *N. Engl. J. Med.* **360:** 1518–1525.
10. Hu, H. H., and V. Gilsanz. 2011. Developments in the imaging of brown adipose tissue and its associations with muscle, puberty, and health in children. *Front. Endocrinol. (Lausanne).* **2:** 33.
11. Chen, Y. C., A. M. Cypess, M. Palmer, G. Kolodny, C. R. Kahn, and K. K. Kwong. 2013. Measurement of human brown adipose tissue volume and activity using anatomic MR imaging and functional MR imaging. *J. Nucl. Med.* **54:** 1584–1587.
12. Cypess, A. M., C. R. Haft, M. R. Laughlin, and H. H. Hu. 2014. Brown fat in humans: consensus points and experimental guidelines. *Cell Metab.* **20:** 408–415.
13. Hu, H. H., T. G. Perkins, J. M. Chia, and V. Gilsanz. 2013. Characterization of human brown adipose tissue by chemical-shift water-fat MRI. *AJR Am. J. Roentgenol.* **200:** 177–183.
14. Chen, Y. I., A. M. Cypess, C. A. Sass, A-L. Brownell, K. T. Jokivarsi, C. R. Kahn, and K. K. Kwong. 2012. Anatomical and functional assessment of brown adipose tissue by magnetic resonance imaging. *Obesity (Silver Spring).* **20:** 1519–1526.
15. Hu, H. H., T. W. Wu, L. Yin, M. S. Kim, J. M. Chia, T. G. Perkins, and V. Gilsanz. 2014. MRI detection of brown adipose tissue with low fat content in newborns with hypothermia. *Magn. Reson. Imaging.* **32:** 107–117.
16. Branca, R. T., and W. S. Warren. 2011. In vivo brown adipose tissue detection and characterization using water-lipid intermolecular zero-quantum coherences. *Magn. Reson. Med.* **65:** 313–319.
17. Branca, R. T., and W. S. Warren. 2011. In vivo NMR detection of diet-induced changes in adipose tissue composition. *J. Lipid Res.* **52:** 833–839.
18. Bao, J., X. Cui, S. Cai, J. Zhong, C. Cai, and Z. Chen. 2013. Brown adipose tissue mapping in rats with combined intermolecular double-quantum coherence and Dixon water-fat MRI. *NMR Biomed.* **26:** 1663–1671.

19. Le Bihan, D. 1995. Molecular diffusion, tissue microdynamics and microstructure. *NMR Biomed.* **8:** 375–386.
20. Einstein, A. 1905. Über die von der molekularkinetischen Theorie der Wärme geforderte Bewegung von in ruhenden Flüssigkeiten suspendierten Teilchen. *Ann. Phys.* **322:** 549–560.
21. Valencia, D. P., and F. J. González. 2011. Understanding the linear correlation between diffusion coefficient and molecular weight. A model to estimate diffusion coefficients in acetonitrile solutions. *Electrochem. Commun.* **13:** 129–132.
22. Perez, E. E., A. A. Carelli, and G. H. Crapiste. 2011. Temperature-dependent diffusion coefficient of oil from different sunflower seeds during extraction with hexane. *J. Food Eng.* **105:** 180–185.
23. von Smoluchowski, M. 1906. Zur kinetischen Theorie der Brownschen Molekularbewegung und der Suspensionen. *Ann. Phys.* **326:** 756–780.
24. Cao, P., and E. X. Wu. 2016. In vivo diffusion MRS investigation of non-water molecules in biological tissues. *NMR Biomed.* .
25. Cao, P., S. J. Fan, A. M. Wang, V. B. Xie, Z. Qiao, G. M. Brittenham, and E. X. Wu. 2015. Diffusion magnetic resonance monitors intramyocellular lipid droplet size in vivo. *Magn. Reson. Med.* **73:** 59–69.
26. Brandejsky, V., R. Kreis, and C. Boesch. 2012. Restricted or severely hindered diffusion of intramyocellular lipids in human skeletal muscle shown by in vivo proton MR spectroscopy. *Magn. Reson. Med.* **67:** 310–316.
27. Murday, J. S., and R. M. Cotts. 1968. Self-diffusion coefficient of liquid lithium. *J. Chem. Phys.* **48:** 4938.
28. Packer, K., and C. Rees. 1972. Pulsed NMR studies of restricted diffusion. I. Droplet size distributions in emulsions. *J. Colloid Interface Sci.* **40:** 206–218.
29. Garasanin, T., T. Cosgrove, L. Marteaux, A. Kretschmer, A. Goodwin, and K. Zick. 2002. NMR self-diffusion studies on PDMS oil in water emulsion. *Langmuir.* **18:** 10298–10304.
30. Fieber, W., V. Hafner, and V. Normand. 2011. Oil droplet size determination in complex flavor delivery systems by diffusion NMR spectroscopy. *J. Colloid Interface Sci.* **356:** 422–428.
31. Dorfman, S. E., D. Laurent, J. S. Gounarides, X. Li, T. L. Mullarkey, E. C. Rocheford, F. Sari-Sarraf, E. A. Hirsch, T. E. Hughes, and S. R. Commerford. 2009. Metabolic implications of dietary trans-fatty acids. *Obesity (Silver Spring).* **17:** 1200–1207.
32. Greenberg, A. S., R. A. Coleman, F. B. Kraemer, J. L. McManaman, M. S. Obin, V. Puri, Q-W. Yan, H. Miyoshi, and D. G. Mashek. 2011. The role of lipid droplets in metabolic disease in rodents and humans. *J. Clin. Invest.* **121:** 2102–2110.
33. Chiu, H. C., A. Kovacs, D. A. Ford, F. F. Hsu, R. Garcia, P. Herrero, J. E. Saffitz, and J. E. Schaffer. 2001. A novel mouse model of lipotoxic cardiomyopathy. *J. Clin. Invest.* **107:** 813–822.
34. Doty, F. D., G. Entzminger, and Y. A. Yang. 1998. Magnetism in high-resolution NMR probe design. I: general methods. *Concepts Magn. Reson.* **10:** 133–156.
35. Sprinkhuizen, S. M., C. J. G. Bakker, J. H. Ippel, R. Boelens, M. A. Viergever, and L. W. Bartels. 2012. Temperature dependence of the magnetic volume susceptibility of human breast fat tissue: an NMR study. *MAGMA.* **25:** 33–39.
36. Wu, D. H., A. D. Chen, and C. S. Johnson. 1995. An improved diffusion-ordered spectroscopy experiment incorporating bipolar-gradient pulses. *J. Magn. Reson. A.* **115:** 260–264.
37. Stejskal, E. O., and J. E. Tanner. 1965. Spin diffusion measurements: spin echoes in the presence of a time-dependent field gradient. *J. Chem. Phys.* **42:** 288.
38. Mills, R. 1973. Self-diffusion in normal and heavy water in the range 1–45°. *J. Phys. Chem.* **77:** 685–688.
39. Holz, M., and H. Weingartner. 1991. Calibration in accurate spin-echo self-diffusion measurements using ^{1}H and less-common nuclei. *J. Magn. Reson.* **92:** 115–125.
40. Mosconi, E., M. Fontanella, D. M. Sima, S. Van Huffel, S. Fiorini, A. Sbarbati, and P. Marzola. 2011. Investigation of adipose tissues in Zucker rats using in vivo and ex vivo magnetic resonance spectroscopy. *J. Lipid Res.* **52:** 330–336.
41. Lim, S., J. Honek, Y. Xue, T. Seki, Z. Cao, P. Andersson, X. Yang, K. Hosaka, and Y. Cao. 2012. Cold-induced activation of brown adipose tissue and adipose angiogenesis in mice. *Nat. Protoc.* **7:** 606–615.
42. Schindelin, J., I. Arganda-Carreras, E. Frise, V. Kaynig, M. Longair, T. Pietzsch, S. Preibisch, C. Rueden, S. Saalfeld, B. Schmid, et al. 2012. Fiji: an open-source platform for biological-image analysis. *Nat. Methods.* **9:** 676–682.
43. Galarraga, M., J. Campion, A. Munoz-Barrutia, N. Boque, H. Moreno, J. A. Martinez, F. Milagro, and C. Ortiz-de-Solorzano. 2012. Adiposoft: automated software for the analysis of white adipose tissue cellularity in histological sections. *J. Lipid Res.* **53:** 2791–2796.
44. Tanner, J. E. 1968. Restricted self-diffusion of protons in colloidal systems by the pulsed-gradient, spin-echo method. *J. Chem. Phys.* **49:** 1768.
45. Callaghan, P. T. 1991. Principles of Nuclear Magnetic Resonance Microscopy. Clarendon Press, Oxford, UK.
46. Johnson, C. S. 1993. Effects of chemical exchange in diffusion-ordered 2D NMR spectra. *J. Magn. Reson. A.* **102:** 214–218.
47. Cain, J. B., K. Zhang, D. E. Betts, J. M. DeSimone, and C. S. Johnson. 1998. Diffusion of block copolymers in liquid CO_2 : evidence of self-assembly from pulsed field gradient NMR. *J. Am. Chem. Soc.* **120:** 9390–9391.
48. Borga, M., K. A. Virtanen, T. Romu, O. D. Leinhard, A. Persson, P. Nuutila, and S. Enerbäck. 2014. Brown adipose tissue in humans: detection and functional analysis using PET (positron emission tomography), MRI (magnetic resonance imaging), and DECT (dual energy computed tomography). *Methods Enzymol.* **537:** 141–159.
49. Zhang, X., C. Kuo, A. Moore, and C. Ran. 2013. In vivo optical imaging of interscapular brown adipose tissue with ^{18}F-FDG via Cerenkov luminescence imaging. *PLoS One.* **8:** e62007.
50. Hamilton, G., D. L. Smith, M. Bydder, K. S. Nayak, and H. H. Hu. 2011. MR properties of brown and white adipose tissues. *J. Magn. Reson. Imaging.* **34:** 468–473.
51. Hu, H. H., C. D. G. Hines, D. L. Smith, and S. B. Reeder. 2012. Variations in T_2* and fat content of murine brown and white adipose tissues by chemical-shift MRI. *Magn. Reson. Imaging.* **30:** 323–329.
52. Zancanaro, C., R. Nano, C. Marchioro, A. Sbarbati, A. Boicelli, and F. Osculati. 1994. Magnetic resonance spectroscopy investigations of brown adipose tissue and isolated brown adipocytes. *J. Lipid Res.* **35:** 2191–2199.
53. Steidle, G., F. Eibofner, and F. Schick. 2011. Quantitative diffusion imaging of adipose tissue in the human lower leg at 1.5 T. *Magn. Reson. Med.* **65:** 1118–1124.
54. Gennis, R. B. 1989. Biomembranes: Molecular Structure and Function. Springer Verlag, New York, NY. 168–198.
55. Guilherme, A., J. V. Virbasius, V. Puri, and M. P. Czech. 2008. Adipocyte dysfunctions linking obesity to insulin resistance and type 2 diabetes. *Nat. Rev. Mol. Cell Biol.* **9:** 367–377.